

IMECE2011-64352

A COMPUTATIONAL VALIDATION OF TURBINE NOZZLE GUIDE VANE AERODYNAMIC EXPERIMENTS IN AN HP TURBINE STAGE

Özhan H. Turgut*

Turbomachinery Aero-Heat Transfer Laboratory
 Department Aerospace Engineering
 The Pennsylvania State University
 University Park, Pennsylvania 16802
 Email: oht101@psu.edu

Cengiz Camci†

Turbomachinery Aero-Heat Transfer Laboratory
 Department Aerospace Engineering
 The Pennsylvania State University
 University Park, Pennsylvania 16802
 Email: cxc11@psu.edu

ABSTRACT

A computational validation study related to aerodynamic loss generation mechanisms is performed in an axial flow turbine nozzle guide vane (NGV). The 91.66 cm diameter axial flow turbine research facility has a stationary nozzle guide vane assembly and a 29 bladed HP turbine rotor. The NGV inlet and exit Reynolds numbers based on midspan axial chord are around 300000 and 900000, respectively. The effect of grid structure on aerodynamic loss generation is investigated. GAMBIT and TGRID combination is used for unstructured grid, whereas GRID-PRO is the structured grid generator. For both cases, y^+ values are kept below unity. The finite-volume flow solver ANSYS CFX with SST $k - \omega$ turbulence model is employed. Experimental flow conditions are imposed at the boundaries. The flow transition effect and the influence of corner fillets at the vane-endwall junction are also studied in this paper. Grid independence study is performed with static pressure coefficient distribution at the midspan of the vane and the total pressure coefficient at the NGV exit. The velocity distributions and the total pressure coefficient at the NGV exit plane are in very good agreement with the experimental data. This validation study shows that the effect of future geometrical modifications on the endwalls and the vane will be predicted reasonably accurately. The current study shows that an accurately measured turbine stage geometry, a properly prepared block structured/body fitted grid, a state of the art transitional flow implementation, and realistic boundary conditions

coming from high resolution turbine experiments are all essential ingredients of a successful NGV aerodynamic loss quantification via computations.

NOMENCLATURE

- c Midspan axial chord length of nozzle guide vane.
- C_P Static Pressure coefficient; $(P_1 - P_2)/(0.5 \rho U_m^2)$.
- C'_P Static Pressure coefficient; $(P - P_{01})/(0.5 \rho V_{x1}^2)$.
- C_{P1} Total pressure coefficient; $(P_{02} - P_{01})/(0.5 \rho U_m^2)$.
- k Turbulence kinetic energy.
- P Static pressure.
- P_0 Total pressure.
- $Re_{\theta t}$ Momentum-thickness Reynolds number.
- T_0 Total temperature.
- U_m Blade speed at mean radius.
- V Velocity magnitude.
- V_x Axial velocity component.
- V_r Radial velocity component.
- V_θ Circumferential velocity component.
- x Axial distance from nozzle guide vane leading edge.
- y^+ Non-dimensional wall coordinate; $\sqrt{\tau_w/\rho} \cdot y_p / v$.
- y_p First grid height off the wall.

Greek

- γ Intermittency.
- ν Kinematic viscosity.
- ρ Density.
- τ_w Wall shear stress.

*Graduate Research Assistant, ASME Student Member

†Professor of Aerospace Engineering, ASME Fellow

ω Turbulent frequency.

Subscripts

- 1 One axial chord upstream of nozzle guide vane leading edge.
- 2 Nozzle guide vane exit plane, $x/c = 1.025$.
- 3 Turbine rotor exit plane.

Abbreviations

- N Turbine nozzle guide vane.
 R Turbine blade.
 SST Shear stress transport.
 TKE Turbulence kinetic energy.

INTRODUCTION

The fluid flow through a turbine nozzle guide vane (NGV) is one of the most complex internal flows that are highly three dimensional and unsteady. The boundary layers in NGV flows may well contain laminar, transitional and fully turbulent flow regimes simultaneously. The high turning angle of the vanes and the momentum deficit in the inlet endwall boundary layer lead to secondary flows with significant mean kinetic energy loss. According to Denton [1], about one third of the total aerodynamic loss in a turbine passage is due to endwall losses. Researchers have been trying to understand the generation mechanisms of secondary flows since 1950's and trying to minimize the losses related to these flows. A comprehensive review by Sieverding [2] presents the experimental measurements on secondary flows and endwall boundary layers until 1985. Later on, Langston [3] reviewed the papers until 2001, which were related to the secondary flows, including the flow structure investigation either by experiments or by numerical methods and new approaches to reduce the secondary flow related losses.

Although experiments provide valuable results in an actual turbine passage, it is time consuming and expensive to set up a full scale turbine experiment under actual operating conditions. On the other hand, analytical approach is a mathematical expression that gives exact solutions to a specified problem. However, not every fluid flow problem has an analytical closed-form expression. The three-dimensional secondary flows in a turbine NGV passage is one of them, therefore, computational fluid dynamics (CFD) is an essential tool for the flow prediction of turbine passages.

Three-dimensional Navier-Stokes equations based CFD using Reynolds averaging has been used as a flow prediction tool for turbine flows since 1980s. Hah [4] developed his three-dimensional compressible Navier-Stokes scheme for turbomachinery applications. Good agreement with measured airfoil static pressure distribution was achieved, however, mass-averaged loss coefficient was over-predicted. Moore and Moore [5] calculated turbine performance by an elliptic flow solver. Mass-averaged total pressure loss values within the passage and downstream of the blade were predicted with good agreement with the measured data. Dorney and Davis [6] analyzed aero-

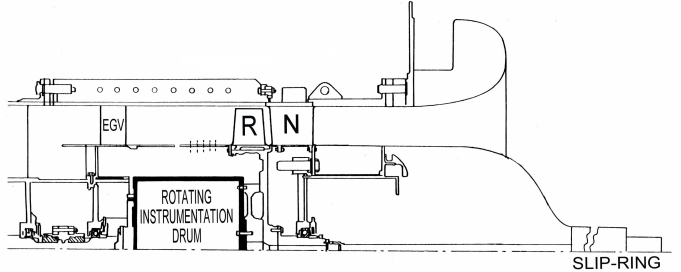


FIGURE 1: The turbine facility sketch.

dynamics and heat transfer for a linear turbine using a three-dimensional Navier-Stokes flow solver. They presented a grid resolution study and importance of the transition modeling. The area-averaged loss was calculated within 2% error margin with the finest grid. Harvey et al. [7] applied non-axisymmetric end-wall contouring to both vane and blade of the Rolls-Royce Trent 500 engine intermediate pressure turbine. Their predicted efficiency improvement is closer to the measured value. Nagel and Baier [8] aimed to rise the efficiency of the turbine NGV by developing a combined design of both vanes and the end wall. A 3D compressible transitional Reynolds Averaged Navier-Stokes (RANS) solver was used for the flow simulation. Airfoil static pressure distribution was in good agreement with measured data. The aerodynamic loss distribution contours and the values are similar to the experimental measurements.

The users of CFD have to admit that it does not provide an exact solution to the fluid flow. There are always errors related to this numerical approach. The types of errors related to CFD simulations governed by partial differential equations (PDE) are discussed in detail by Oberkampf and Blottner [9]. Mainly four types of errors exist: i) errors related to physical modeling, ii) numerical discretization errors, iii) errors in programming, and iv) errors related to computer round-off. Physical modeling errors could arise from the mathematical expressions for viscous/inviscid flows, turbulence modeling, boundary conditions, etc. Errors in discretization of PDEs, turbulence models, boundary conditions, and the resolution of grid may be included in numerical discretization errors.

A more recent study by Denton [10] discusses the types of CFD errors more specific to turbomachinery applications. The types of turbomachinery CFD errors are summarized as numerical errors, modeling errors, errors related to boundary conditions, and the geometrical considerations of the blade, seal and tip clearances, etc. It is suggested that CFD is to be used as a comparison tool, instead of a performance prediction method. It is also noted that CFD should be calibrated based on experiments, not the vice versa.

Keeping in mind the limitations and the errors in CFD prediction, this paper aims to simulate the fluid flow through a tur-

TABLE 1: The AFTRF design performance parameters.

Inlet Total Temperature ($^{\circ}K$); T_{0_1}	289
Inlet Total Pressure (kPa); P_{0_1}	101.36
Mass Flow Rate (kg/s); Q	11.05
Rotational speed (rpm); N	1300
Total Pressure Ratio; P_{0_1}/P_{0_3}	1.0778
Total Temperature Ratio; T_{0_3}/T_{0_1}	0.981
Pressure Drop ($mmHg$); $P_{0_1} - P_{0_3}$	56.04
Power (kW); P	60.6

TABLE 2: The AFTRF design features.

Rotor Hub Tip Ratio	0.7269
Tip Radius (m); R_{tip}	0.4582
Blade Height (m); h	0.1229
Tip Relative Mach Number	0.24 (max)
Nozzle Guide Vane (tip)	
number	23
chord (m)	0.1768
spacing (m)	0.1308
turning angle	70
maximum thickness (mm)	38.81
Midspan Axial Chord	
nozzle (m)	0.1123
rotor (m)	0.09294
Vane Reynolds Number	
based on inlet velocity	$(3 \sim 4) \times 10^5$
based on exit velocity	$(9 \sim 10) \times 10^5$

bine NGV. The experimental facility generating the experimental data sets will be described. The current NGV experiments reported in this paper are all obtained in a single stage HP turbine flow simulator including a 29 bladed rotor section. A comprehensive study will be presented with both unstructured and block-structured body fitted structured meshes. The necessity for high grid resolution near wall boundaries will be discussed. The fluid flow in a turbine NGV is likely to be transitional especially near the suction side of the nozzle guide vanes, as long as the vanes are not film cooled on the gas side. Fully turbulent and transitional flow calculations will be compared and the influence of corner fillets at the vane-endwall junction will be emphasized. The computed NGV exit flow conditions will be compared to the available experimental data of previously obtained in Axial Flow Turbine Research Facility (AFTRF) [11].

EXPERIMENTAL FACILITY

The Axial Flow Turbine Research Facility (AFTRF) installed at the Turbomachinery Aero-Heat Transfer Laboratory of the Pennsylvania State University is a low speed, single-stage, cold flow turbine having a diameter of 91.66 cm. Table 1 summarizes the design performance parameters of the turbine facility and the design features are shown in Tab. 2. The detailed description and the characteristics of the AFTRF can be found in Lakshminarayana et al. [12] and Camci [13]. The facility is driven by four stages of axial suction fans downstream of the rotor section and the speed of the rotor is controlled by a power absorbing eddy-current brake. The inlet section has a bell-mouth shape followed by the NGV row and the rotor blades. A sketch of the AFTRF is given in Fig. 1. There are 23 NGV's and 29 rotor blades followed by the exit guide vanes.

COMPUTATIONAL FEATURES

The viscous flow simulations in this paper are carried out by the finite-volume flow solver ANSYS CFX. The three-dimensional compressible RANS flow equations are solved for steady-state air flow around a single NGV. This specific study does not include the rotor simulation, and hence, the vane-rotor interaction is not investigated at this stage. Rotationally periodic boundary conditions are applied on the side walls of the computational domain. A no-slip, adiabatic wall is selected for vane, hub and casing boundaries. For the inlet boundary, experimental flow conditions measured at one axial chord upstream of the NGV are adapted [14]. The uncertainty values for the experimental data are provided in the Appendix. The velocity magnitude and the turbulent kinetic energy distribution along the span at the inlet is shown in Fig. 2. The total pressure value given as the inlet boundary condition is calculated from the velocity distribution. Total temperature at the inlet is 298.15 K. At the outlet boundary, experimental mass flow rate value is specified.

Two-equation SST $k-\omega$ turbulence model of Menter [15] is selected for all the simulations. This turbulence model is widely used by many researchers to predict the turbine secondary flows. One of the recent studies of a turbine blade simulation with this

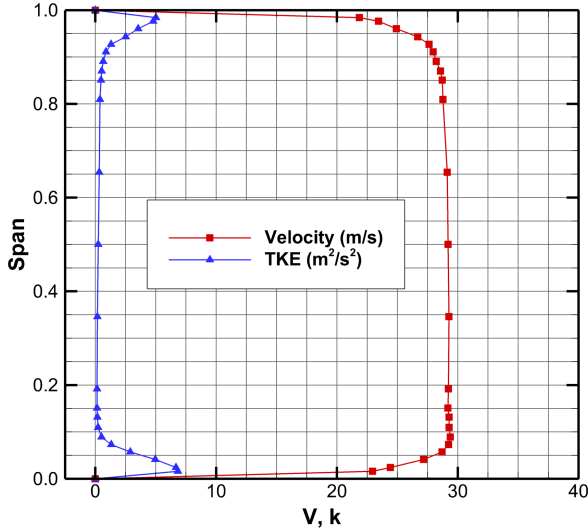


FIGURE 2: Experimental inlet velocity magnitude and turbulent kinetic energy distribution.

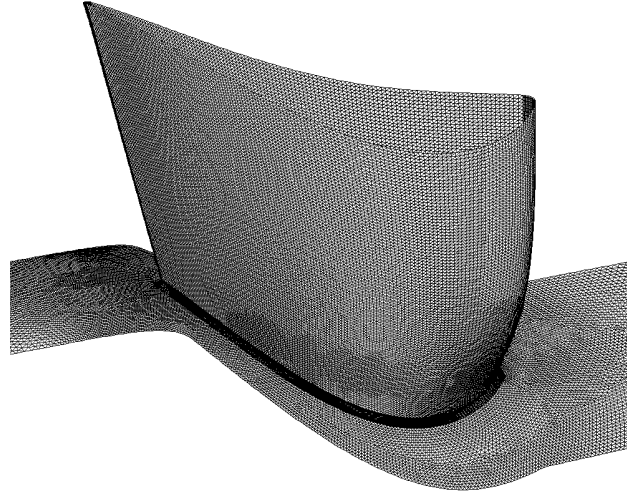


FIGURE 3: Unstructured grid.

turbulence model is discussed in Levchenya et al. [16].

INFLUENCE OF GRID GENERATION AND TRANSITION FLOW MODELING

Throughout this paper, flow simulations with both unstructured and structured grids will be discussed. An unstructured mesh is easy to implement in three-dimensional flows including complex shaped geometries. For instance, flow through an NGV passage could introduce some difficulty in mesh generation because of the vane geometry and the high turning angle of the passage. Unstructured mesh is an automated grid generation that needs little user effort. The two-dimensional mesh on the boundaries are created first and inside of the computational volume is filled arbitrarily with tetrahedra. However, arbitrariness of the tetrahedron cells requires additional flow solver time and computational memory for the connection of the non-orderly created neighboring cells. Moreover, the tetrahedron cells are insufficient in capturing the flow physics within the boundary layer. Prisms should be used within the boundary layer to better resolve the near wall flow physics.

On the other hand, a structured grid has hexahedral elements which are created in an orderly pattern within the computational volume. User can easily modify grid density at the specific regions of the flow (*i.e.* wake of a blade). The drawback of this method is for complex geometries, it is very difficult to form a single block structured mesh. Users should split the computational domain into several blocks, which is called multi-block structured mesh generation.

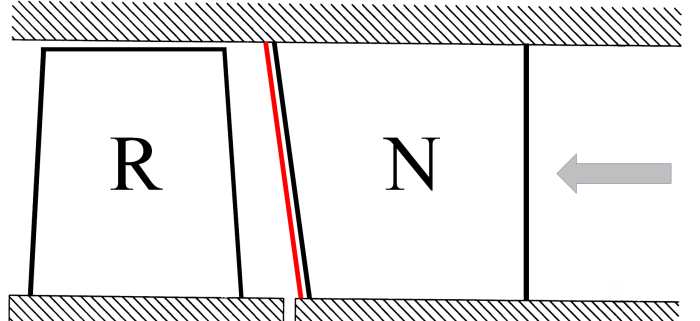
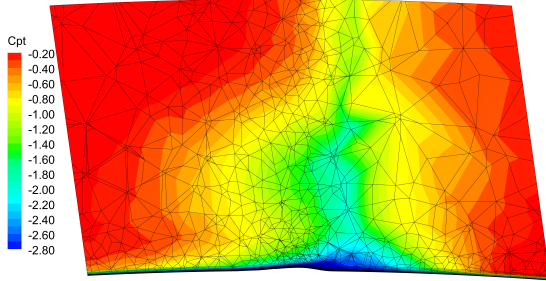


FIGURE 4: NGV exit plane.

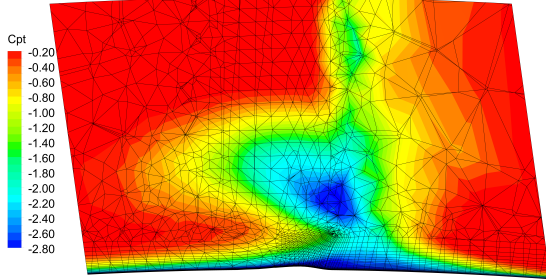
Unstructured Grid Generation

The unstructured grid generation in this study involves two steps. First step is to mesh the boundaries of the whole domain. GAMBIT is used as a surface mesh generator. An example of this boundary grid is depicted in Fig. 3. As the second step, this surface mesh is imported in TGRID. Then, prism layers are developed from this boundary mesh perpendicular to the walls. It is crucial to use prisms to resolve the near wall gradients. The crossflows within the NGV passage is mainly due to the velocity magnitude differences within the boundary layer. If a proper near wall grid resolution is not achieved, then the simulation results will diverge from the experiments.

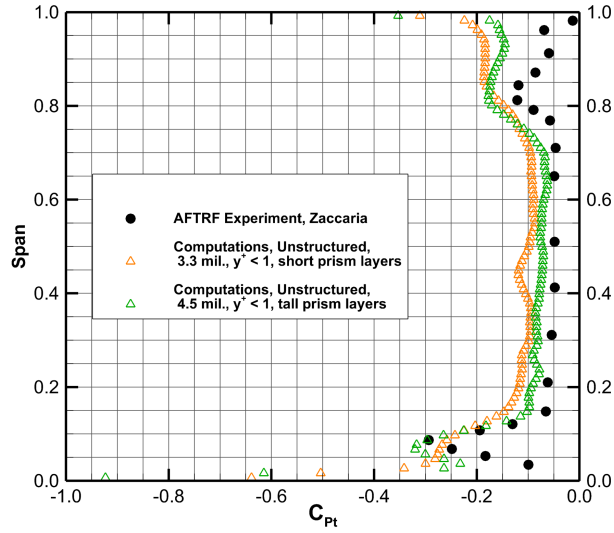
To examine the effect of the number of prism layers created, the total pressure coefficient, C_{Pt} , is compared at the NGV



(a) 3.3 million mesh with short prism layers



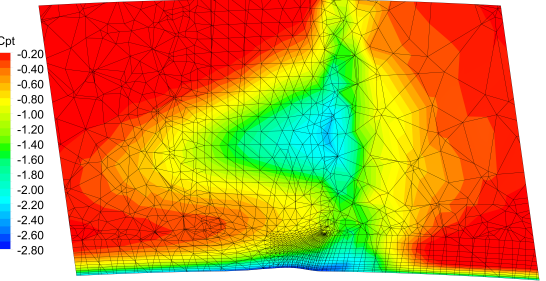
(b) 4.5 million mesh with tall prism layers



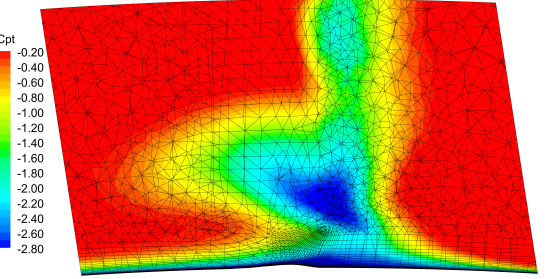
(c) Spanwise distribution of total pressure coefficient

FIGURE 5: Prediction of total pressure loss and comparison with experimental data [11], effect of prism layer height on unstructured mesh at NGV exit plane.

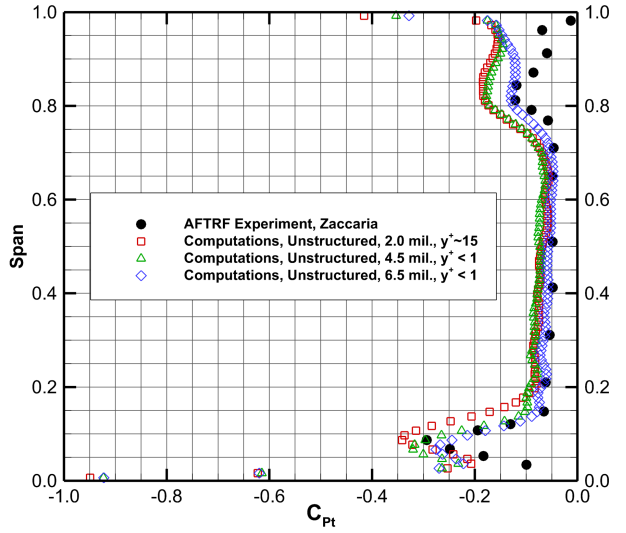
exit plane, which is shown in Fig. 4 by the red solid line drawn parallel to the NGV trailing edge. Two different unstructured mesh results are presented in Fig. 5. These C_{Pt} contours are plotted up to 20% span of the vane. To clarify the position of these contour plots, it should be pointed out that the flow to the left of wake region comes from the suction surface of the vane.



(a) 2.0 million mesh



(b) 6.5 million mesh



(c) Spanwise distribution of total pressure coefficient

FIGURE 6: Prediction of total pressure loss and comparison with experimental data [11], unstructured mesh comparison at NGV exit plane.

Note that, Fig. 5a and Fig. 5b do not have the same number of mesh sizes. The reason is, when comparing these two cases, all the parameters within TGRID are kept constant (*i.e.* boundary mesh, $y^+ < 1$, growth ratio of the tetrahedra within the volume), except the number of prism layers. The importance of resolving the near wall grid is clear as shown in Fig. 5b. The core

of the secondary flow and the separation of the secondary flows from the endwall is well captured. The spanwise distribution of the circumferentially mass-averaged total pressure coefficient is compared to AFTRF measurements in Fig. 5c. The one with tall prism layers qualitatively predicts the secondary flow areas, but there is still an offset from the experimental data. The wake is not predicted well, that is due to the coarse mesh in that region. The secondary flow region is not distinguishable in short prism layer results. The endwall loss and the secondary flow loss is mixed to each other. This study showed that when using an unstructured mesh, the prism layer plays an important role in calculating the gradients within the boundary layer.

After investigating the influence of prism layers, two more unstructured meshes are examined with tall prism layers. Boundary mesh is the same with the ones used above. TGRID is an automatic mesh generator that fills the computational volume with tetrahedra using a specified growth ratio. The growth ratio defines the expanding of the tetrahedron cells starting from the boundary mesh. The next unstructured grid has $y^+ \sim 15$ at the first grid point near the wall and a default growth ratio of 1.6 resulting in total of 2 million cells. The C_{P_t} contours in Fig. 6a (2 million cells) show that the core of the secondary flow region is shifted up in the spanwise direction. The minimum value of C_{P_t} is around -2.2, whereas it is around -2.8 in Fig. 5b. Additionally, the secondary flow area in Fig. 6a is wider both in circumferential and spanwise direction. The pressure side of the wake is still not simulated properly. The wake near the pressure side is unnecessarily spilled towards the core flow because of the relatively coarse grid structure. It is concluded that, more cells are needed in the domain, especially near the pressure side of the wake and in the secondary flow zone near the suction side at the NGV exit. Moreover, $y^+ < 1$ at the first grid point is an essential grid resolution near the wall to calculate the flow physics within the boundary layer especially in transitional boundary layers and heat transfer problems. The wall function approach is not suitable according to the discussion of Oberkampf and Blottner [9]. Even though the wall function approach reduces the size of the grid required, the velocity gradients may not be captured accurately in the logarithmic layer, especially when there is separation near the wall.

The last unstructured grid as shown in Fig. 6b has $y^+ < 1$ at the first grid point near the wall with a growth ratio of 1.1, having 6.5 million cells in total. The total pressure contours are smoother, and the wake is well predicted. The circumferentially mass-averaged distribution of C_{P_t} along the span is depicted in Fig. 6c. The core of the secondary flow region is predicted closer to the wall when compared to the experimental data. Even though this 6.5 million cell grid simulates the NGV passage flow properly, the necessity of large computational memory and time concerns come into the picture. The authors of this paper decided to switch to body fitted block structured grid for time efficient and well predicted computational simulations. The structured

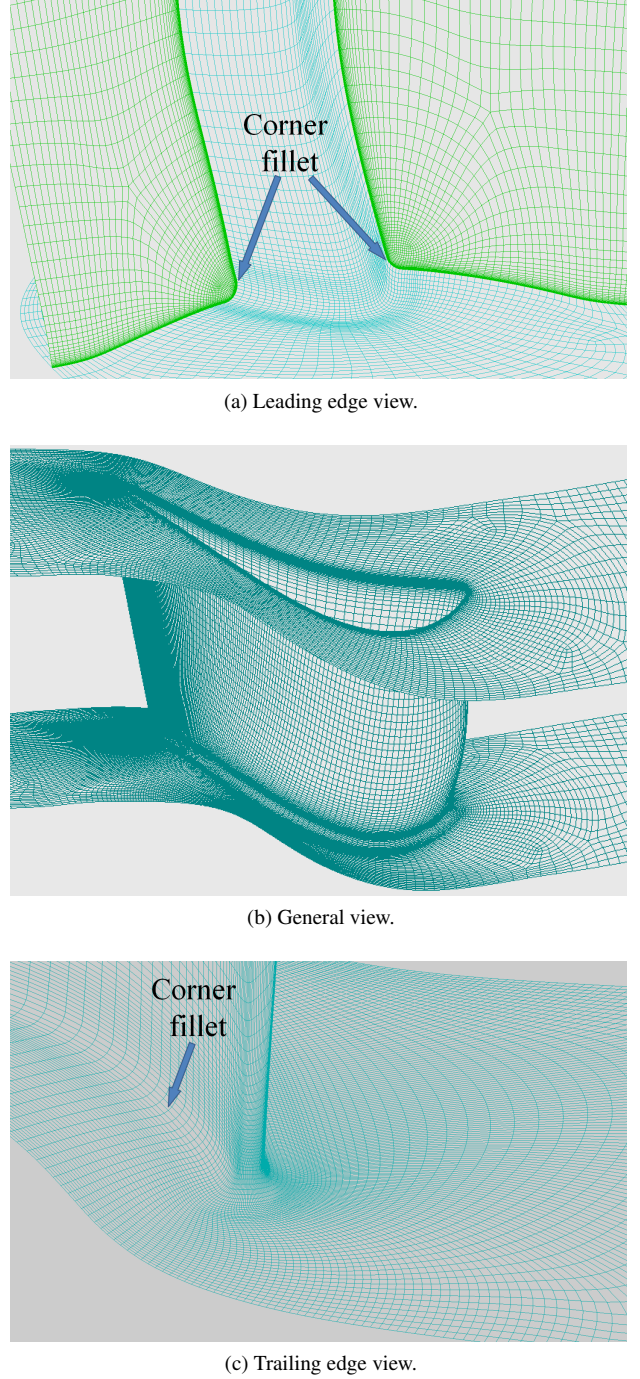


FIGURE 7: Block structured body-fitted mesh.

grid based flow simulations will be introduced and discussed in the next section.

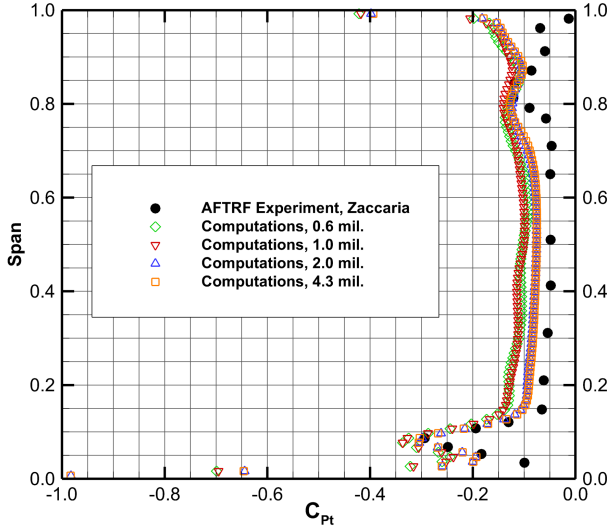


FIGURE 8: Grid independence study on C_{Pt} at NGV exit without transition model, comparison with experimental data [11].

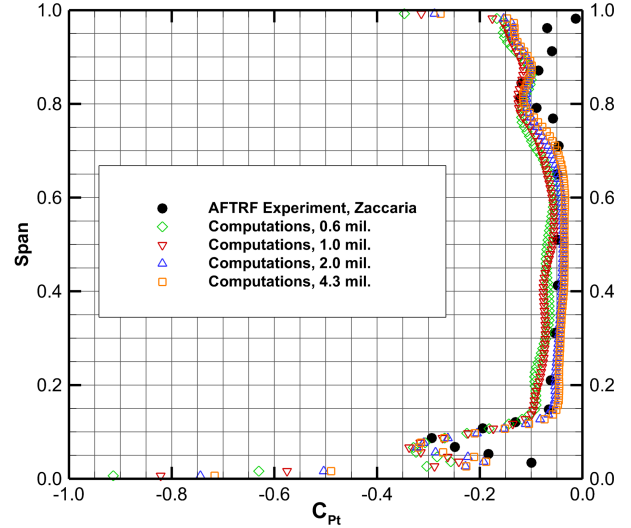


FIGURE 9: Grid independence study on C_{Pt} at NGV exit with transition model, comparison with experimental data [11].

Structured Grid Analysis with Transitional Flow Modeling

A grid independence study is performed with different sizes of structured grid. As noted previously, for complex geometries, it may be beneficial to use a multi-block grid strategy to create a mesh orthogonal to the boundaries. GRIDPRO is selected as the grid generator. A sample grid at the NGV leading edge and a perpendicular plane within the passage is shown in Fig. 7. From the previous section it was learned that the near wall grid resolution is important, therefore, $y^+ < 1$ is assured with the structured grid as well.

The first results with a structured grid is obtained with fully turbulent flow assumption starting from the inlet of the computational domain. Transition criteria is not taken into account. Four different structured mesh sizes are compared, namely 0.6, 1.0, 2.0, and 4.3 million cells. The circumferentially mass-averaged total pressure coefficient distribution at the NGV exit is plotted in Fig. 8. The first important item to notice in this figure is that the profile losses of the NGV are not accurately predicted. For the 2.0 and 4.3 million cell grids the error is around 50% and for 0.6 and 1.0 million cell grids it is around 100%. These errors appear to be very large, but note that, the C_{Pt} value at the midspan is approximately -0.05. As for the grid independence, it is clear from the figure that 2.0 and 4.3 million cells are giving the similar results. The aerodynamic losses are over-predicted especially in the profile loss zone. Whereas, for the 0.6 and 1.0 million cell grids, the over-prediction of the total pressure is much more exaggerated. For instance, from the hub to 7% span location, there is a $\Delta C_{Pt} = 0.05$ between coarse mesh (0.6 and 1.0 mil-

lions cells) and fine mesh (2.0 and 4.3 million mesh). Although this figure gives an important information on grid independence, the authors still think that this is not a reliable CFD prediction for future calculations. The simulations seem to be grid independent after a grid size of 2 million cells, however the accuracy of these seemingly grid independent simulations are questionable.

Mayle [17] states that the flow over an uncooled turbine NGV or blade can be transitional. The transition phenomenon in gas turbines is thoroughly discussed in [17]. It is concluded that the transition is mainly dominated by the free-stream turbulence level, x Reynolds number, pressure gradient, and unsteady wake passing. The influence of heat transfer, surface curvature, surface roughness, and the compressibility on the transition are not as much as free-stream turbulence level. Denton [10] argues that an inaccurate specification of the transition point, instead of predicting it within the calculation, may lead to weak quantification of turbine efficiency.

Many researchers tried to predict transition within the two equation turbulence models. Another approach is to employ empirical correlations as transition models. The Gamma Theta Model in CFX uses a built-in correlation. In this model two extra transport equations are solved, one for the intermittency (γ) and the other for momentum thickness Reynolds number (Re_{θ_t}). SST turbulence model with this correlation is validated for various transitional flow cases [18, 19, 20].

In the present study, the Gamma Theta Model is selected as the transitional flow model. The same structured grids are used to observe the transitional effects. The total pressure coefficient distribution at NGV exit plane is presented in Fig. 9.

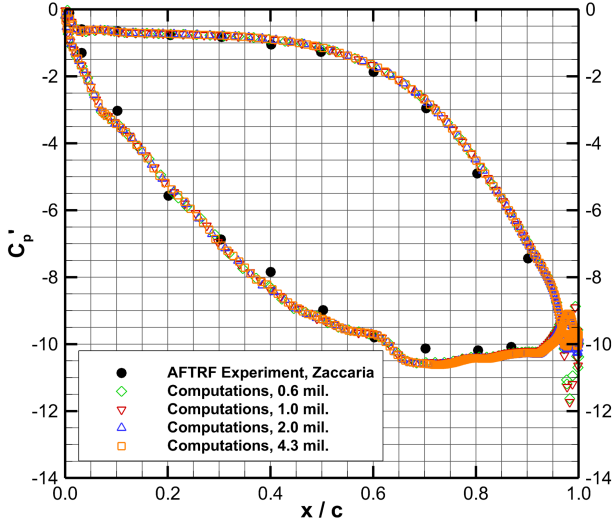


FIGURE 10: Grid independence study on C'_P at midspan with transition model, comparison with experimental data [11].

2.0 and 4.3 million grid predicts C_{Pt} very close to experimental data along the wake and in the secondary flow zone near the hub. One should notice that the secondary flow measurements near the casing carry slightly more uncertainty because of the probe insertion slot related disturbances on the turbine casing at the exit of the NGV. This paper consistently uses the hub secondary flow measurements for comparative purposes. On the other hand, the grids with 0.6 and 1.0 million cells are not capable of capturing the wake profile and the profile losses. Moreover, there is again a difference of $\Delta C_{Pt} = 0.05$ up to 6% span between the coarse (0.6 and 1.0 million) and fine mesh (2.0 and 4.3 million). There is also a relatively weak comparison for all structured grids above 90% span of the vane. The main reason for this mismatch is the existence of an open slot on the experimental facility that the probe could traverse. Although a significant technical effort is made to minimize this slot influence, a complete elimination of its influence is not the case. This opening creates a suction near the casing area, energizing the fluid very close to the wall, and reducing the measured losses. In CFD calculations this slot is not taken into account, and therefore the total pressure loss is calculated higher than the experimental data.

The midspan pressure coefficient distribution on the blade surface is shown in Fig. 10. All the structured grid configurations calculate similar C_P values and they are all in very good agreement with the experimental measurement. Note that, very close to the trailing edge region, the C_P distribution indicates a negative loading. This behavior is well described by Denton [10]. If a very fine grid is used near the trailing edge, the flow separation is delayed, which is supposed to be at the pressure surface and trail-

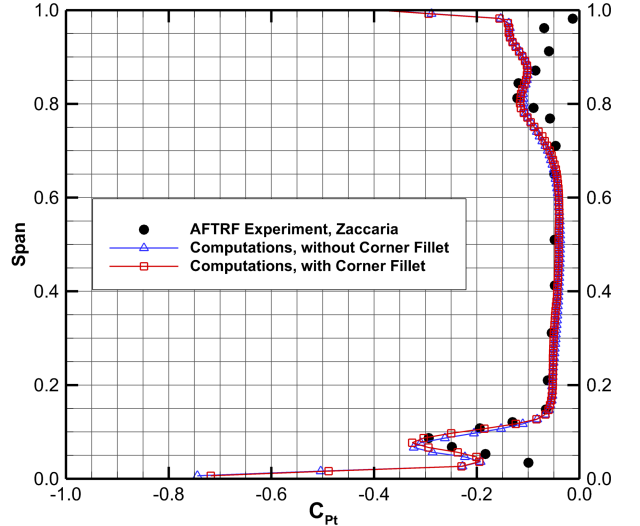


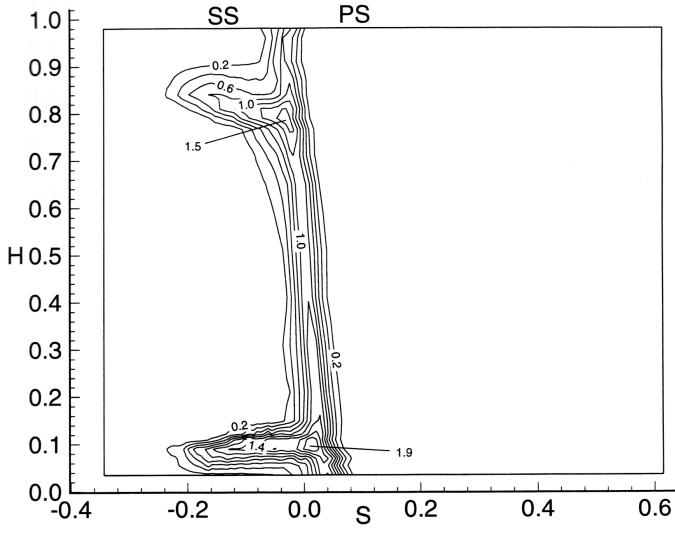
FIGURE 11: Effect of corner fillet, comparison with experimental data [11].

ing edge junction. The flow remains reattached and accelerates around the trailing edge, causing a pressure drop.

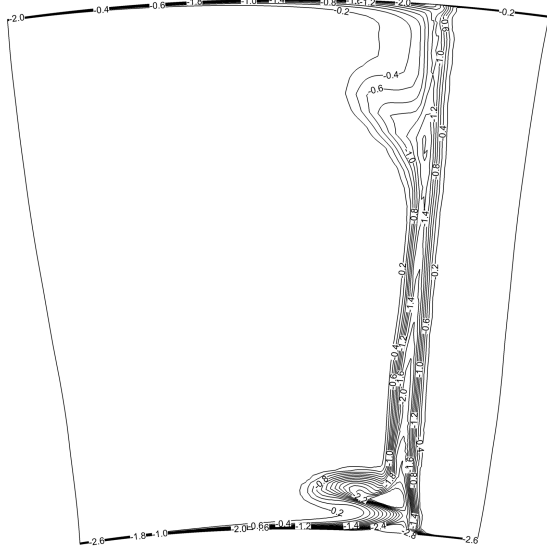
One of the goals of this study is to capture the secondary flows in the NGV passage and the related total pressure loss at the NGV exit. Fig. 10 tells that even a 0.6 million cells grid structure accurately predicts the static pressure coefficient at midspan. However, it is obvious from Fig. 9 that the calculation seems grid dependent for the total pressure coefficient prediction below 2.0 million cells. For time considerations and the computer resources, the authors of this paper selected the 2.0 million cells grid structure as a sufficient mesh resolution for resolving the flow physics.

INFLUENCE OF CORNER FILLET

The results of structured grids discussed previously did not include the corner fillet. This is, in other words, the fillet at the junction of the vane airfoil and the hub endwall. In actual experiments, this fillet was there, and all the measured data includes the effect of this fillet. Germain et al. [21] also states that the fillet has an important role in total pressure coefficient distribution. To investigate the influence of corner fillet in CFD calculations, a structured grid is generated in such a way that fillet is also taken into account. The structured grid, including the corner fillet, is shown in Fig. 7. GRIDPRO is capable of mapping the grid to such fillets and creating orthogonal mesh. Clearly, the corner fillet changes the distribution of the C_{Pt} along the span as shown in Fig. 11. From 4% to 12% span, the distribution is shifted up approximately 1% of the vane height in the spanwise direction.



(a) AFTRF Experiments, Zaccaria [11]



(b) Computational results

FIGURE 12: NGV exit plane total pressure coefficient contours.

Above 12% of the span both cases calculated similar values. The results with corner fillet, especially within the secondary flow region, came out to be in more agreement with the experimental data than the results without corner fillet.

The contour plots of total pressure coefficient at NGV exit plane for experimental measurement and CFD calculation are given in Figs. 12a and 12b. The C_{Pt} values in Figs 12a are positive due to the definition of the expression given by [11]. The total pressure coefficient was defined as $C_{Pt} = (P_0 - P_0)/(0.5 \times$

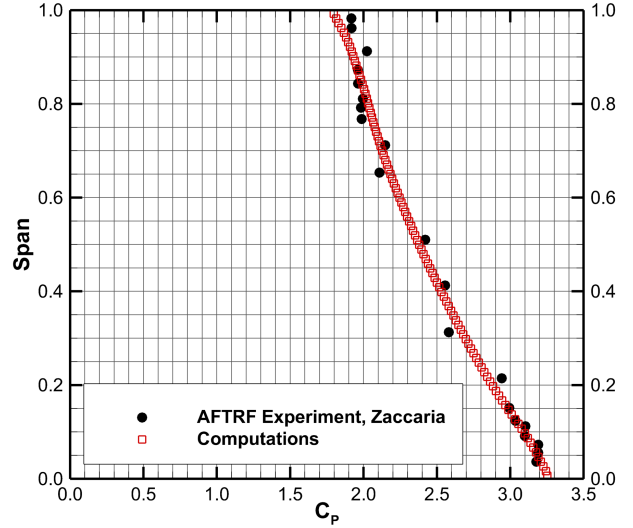


FIGURE 13: Static pressure coefficient at NGV exit plane, comparison with experimental data [11].

$\rho \times U_m^2)$ which had a reverse sign of our definition. So, when comparing these two figures, readers should keep in mind that the contour levels are the same except the sign. Qualitatively, the contour lines show similar behavior. The minimum C_{Pt} value for experimental result is around -1.9, whereas, for computational result it is more than -2.8. But, the circumferentially mass-averaged values are corresponding to each other as was shown in Fig. 11.

The static pressure distribution along the span is given in Fig. 13. The mass-averaged experimental distribution is somewhat scattered along the span, nevertheless, the computational result is following the meanline of the scattered data. Moreover, the three components of computed velocity, namely axial, radial and circumferential, and the velocity magnitude are plotted in Fig. 14. All the data, except the radial component, are in very good agreement with experimental measurements. But note that, the non-dimensional radial component is around zero, and the difference of $V/U_m \approx 0.05$ corresponds to a value of approximately 2.5 m/s .

FLOW VISUALIZATION

Flow visualization results are presented in Fig. 15. The comparison between the streamlines near the endwall and at the midspan is shown in Figs. 15a and 15b. Clearly, the existence of the endwall boundary layer changes the paths of the streamlines which are closer to the hub endwall. The flow particles with lower velocity magnitudes on the pressure side of the passage tend to move towards the suction side of the vane. That trend is

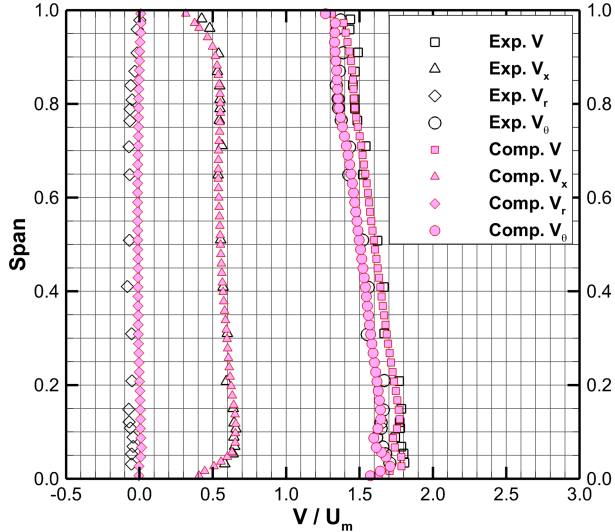
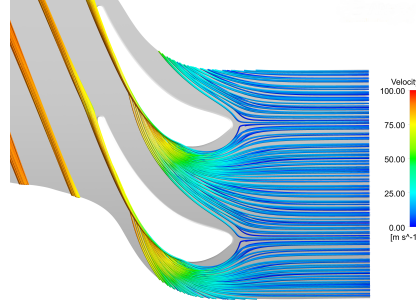


FIGURE 14: Velocity components at NGV exit plane, comparison with experimental data [11].

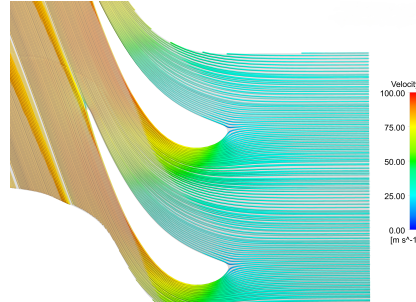
not seen near the midspan. The flow trajectories smoothly follow the vane boundaries without any deflection.

To see the effect of endwall boundary layer in more detail, streamlines are released on a vertical line from hub to 5% span at the inlet boundary, as shown in Figs 15c and 15d. The streamlines with red and yellow colors are directed to the suction side, green and light blue colored ones go to the pressure side of the vane. The yellow streamlines, which are in the boundary layer with lower velocity magnitudes, change their path to the suction side near the minimum pressure point and rise on the vane surface. Meanwhile, the red ones follow their trajectory with minimum deflection. The pressure side streamlines have similar trend. Again, the light blue ones within the boundary layer are deflected towards the suction side surface. But note that, the green streamlines which are released just above the light blue ones, tend to fill the gap of the deflected light blue streamlines. As the flow approaches to the end of the passage, both the green and the light blue ones move beneath the red streamlines and meet with the yellow ones.

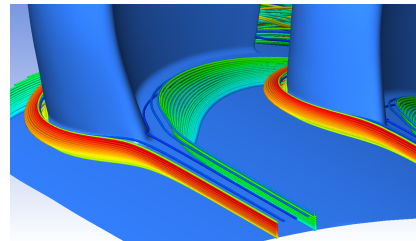
The vortex core regions are presented in Fig. 16. Q -Criterion is selected as the method to isolate secondary flows. It is defined as the second invariant of the velocity gradient tensor. This method is developed by Hunt et al. [22], and the positive values of Q indicates vortex regions. There are two secondary flow regions on the suction side surface of the vane; one closer to the hub, and the other closer to the casing. The horseshoe vortex divides into two parts, suction side leg and the pressure side leg. The suction side leg reattaches to the suction surface near the minimum pressure point, and rises on the surface through the



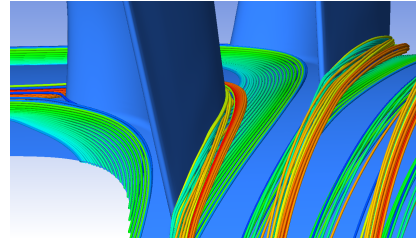
(a) Streamlines released from inlet 1% span.



(b) Streamlines released from inlet 50% span.



(c) Streamlines released from inlet, from hub to 5% span, leading edge view.



(d) Streamlines released from inlet, from hub to 5% span, trailing edge view.

FIGURE 15: Flow visualization in NGV passage.

midspan. The effect of crossflows from the pressure side to the suction side is clear on the casing. There are two distinct secondary flow structures near the casing. One is the suction side leg of the horseshow vortex, which moved towards the midspan, and the other one is generated from the crossflows.

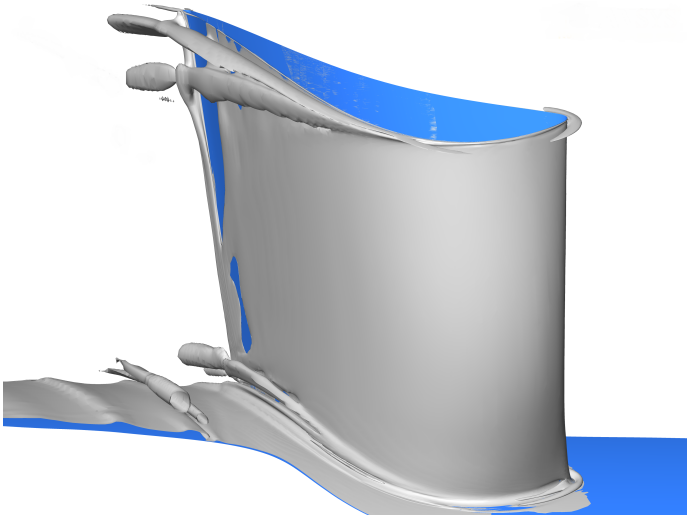


FIGURE 16: Vortex cores.

CONCLUSIONS

The viscous 3D flow through an NGV passage has been simulated. Computational validation study was carried on with both unstructured and structured grids. From the unstructured grid results, it was concluded that the number of prism layers influences the calculation of the gradients within the boundary layer. Additionally, a high grid resolution near the wall was suggested. Another important conclusion from the unstructured grid study was that a finer mesh was needed around the wake and secondary flow regions. As the mesh size was increased, the prediction of the total pressure coefficient values approached to the experimental data. On the other hand, increasing the mesh size brought on other difficulties such as computational memory and time. Hence, the authors of this paper suggested to use block structured body-fitted grids for reasonably accurate CFD simulation of NGV flows in an HP turbine stage.

The fully turbulent computations failed to predict the profile losses or the wake loss of the NGV. Knowing that the suction side of this uncooled NGV airfoil may have a long laminar flow zone after the leading edge, the authors decided to simulate the transitional flow features in the computations. Therefore, transitional parameters were taken into account, and hence, wake profile and profile losses were successfully simulated. Another aspect of the structured grid study was the investigation of the corner fillet effect. It was shown that the secondary flow region was shifted about 1% vane span in the spanwise direction, resulting in a better agreement with the experimental measurement. The computed pressure coefficient, three velocity components, and the velocity magnitude at the NGV exit showed good correspondence with the AFTRF aerodynamic experiments performed in our laboratory.

This paper showed that the current computational approach was successful in simulating our turbine experiments. The aerodynamic losses in the NGV passage of the current HP stage were reasonably accurately obtained from computational simulations. The general simulation approach developed in this paper forms a solid foundation for the development of new NGV aerodynamic loss reduction features such as nonaxisymmetric endwall contouring, leading edge fillets and other optimization driven aerodynamic surface modifications.

ACKNOWLEDGMENT

The authors acknowledge the financial support provided by the Siemens Energy Inc. and thank to Dr. Matthew Montgomery, Dr. Prakash Chander, Dr. Michael Crawford, Andrew Lohaus, Anthony Malandra, Ching-Pang Lee, Boris Dobrzynski, Humberto Zuniga, Ken Landis, and Dirk Nuernberger. The authors are thankful to Dr. Ali Aktürk for his support during this study. The authors are also indebted to Dr. Peter R. Eiseman of Program Development Company, LLC for his great help in grid development for our study.

REFERENCES

- [1] Denton, J. D., 1993. "Loss Mechanisms in Turbomachines". *ASME Journal of Turbomachinery*, **115**, pp. 621–650.
- [2] Sieverding, C. H., 1985. "Recent Progress in the Understanding of Basic Aspects of Secondary Flows in Turbine Blade Passages". *ASME Journal of Engineering for Gas Turbines and Power*, **107**(2), pp. 248–257.
- [3] Langston, L. S., 2001. "Secondary Flows in Axial Turbines - A Review". *Heat Transfer in Gas Turbine Systems, Annals of the New York Academy of Sciences*, **934**, pp. 11–26.
- [4] Hah, C., 1984. "A Navier-Stokes Analysis of Three-Dimensional Turbulent Flows Inside Turbine Blade Rows at Design and Off-Design Conditions". *ASME Journal of Engineering for Gas Turbines and Power*, **106**, pp. 421–429.
- [5] Moore, J., and Moore, J. G., 1985. "Performance Evaluation of Linear Turbine Cascades Using Three-Dimensional Viscous Flow Calculations". *ASME Journal of Engineering for Gas Turbines and Power*, **107**, pp. 969–975.
- [6] Dorney, D. J., and Davis, R. L., 1992. "Navier-Stokes Analysis of Turbine Blade Heat Transfer and Performance". *ASME Journal of Turbomachinery*, **114**, pp. 795–806.
- [7] Harvey, N. W., Brennan, G., Newman, D. A., and Rose, M. G., 2002. "Improving Turbine Efficiency Using Non-Axisymmetric End walls: Validation in the Multi-Row Environment and with Low Aspect Ratio Blading". *ASME Paper No. GT-2002-30337*.
- [8] Nagel, M. G., and Baier, R.-D., 2005. "Experimentally

- Verified Numerical Optimization of a Three-Dimensional Parametrized Turbine Vane With Nonaxisymmetric End Walls". *ASME Journal of Turbomachinery*, **127**, pp. 380–387.
- [9] Oberkampf, W. L., and Blottner, F. G., 1998. "Issues in Computational Fluid Dynamics Code Verification and Validation". *AIAA Journal*, **36**(5), pp. 687–695.
- [10] Denton, J. D., 2010. "Some Limitations of Turbomachinery CFD". *ASME Paper No. GT2010-22540*.
- [11] Zaccaria, M., and Lakshminarayana, B., 1995. "Investigation of Three-Dimensional Flowfield at the Exit of a Turbine Nozzle". *Journal of Propulsion and Power*, **11**(1), January–February, pp. 55–63.
- [12] Lakshminarayana, B., Camci, C., Halliwell, I., and Zaccaria, M., 1996. "Design and Development of a Turbine Research Facility to Study Rotor-Stator Interaction Effects". *International Journal of Turbo and Jet Engines*, **13**, pp. 155–172.
- [13] Camci, C., 2004. "Experimental and Computational Methodology for Turbine Tip De-sensitization". *VKI Lecture Series 2004-02*, Turbine Blade Tip Design and Tip Clearance Treatment.
- [14] Zaccaria, M. A., 1994. "An Experimental Investigation Into the Steady and Unsteady Flow Field in an Axial Flow Turbine". PhD Thesis, The Pennsylvania State University, University Park, PA.
- [15] Menter, F. R., 1994. "Two-Equation Eddy-Viscosity Turbulence Models for Engineering Applications". *AIAA Journal*, **32**(8), pp. 1598–1605.
- [16] Levchenya, A. M., Smirnov, E. M., and Zaytsev, D. K., 2009. "Numerical Simulation of the Endwall Heat Transfer in the Langston Cascade". *Int. Symp. on Heat Transfer in Gas Turbine Systems*, 9–14 August, Antalya, Turkey.
- [17] Mayle, R. E., 1991. "The Role of Laminar-Turbulent Transition in Gas Turbine Engines". *ASME Paper No. 91-GT-261*.
- [18] Menter, F. R., Langtry, R. B., Likki, S. R., Suzen, Y. B., Huang, P. G., and Völker, S., 2004. "A Correlation Based Transition Model Using Local Variables Part 1- Model Formulation". *ASME Paper No. GT2004-53452*.
- [19] Langtry, R. B., Menter, F. R., Likki, S. R., Suzen, Y. B., Huang, P. G., and Volker, S., 2004. "A Correlation Based Transition Model Using Local Variables Part 2- Test Cases and Industrial Applications". *ASME Paper No. GT2004-53454*.
- [20] Langtry, R. B., and Menter, F. R., 2005. "Transition Modeling for General CFD Applications in Aeronautics". *AIAA Paper No. 2005-522*.
- [21] Germain, T., Nagel, M., Raab, I., Schuepbach, P., Abhari, R. S., and Rose, M., 2008. "Improving Efficiency of a High Work Turbine Using Non-Axisymmetric Endwalls Part I: Endwall Design and Performance". *ASME Paper No. GT2008-50469*.
- [22] Hunt, J. C. R., Wray, A. A., and Moin, P., 1988. "Eddies, Stream, and Convergence Zones in Turbulent Flows". *Center for Turbulence Research Rep.*, pp. 193–207.

Appendix A: The AFTRF Nozzle Guide Vane

The five section NGV profile is provided in Fig. 17 and Fig. 18 shows the three-dimensional solid model of the vane geometry. For more information about the AFTRF 3D NGV representation please contact C. Camci at cxc11@psu.edu.

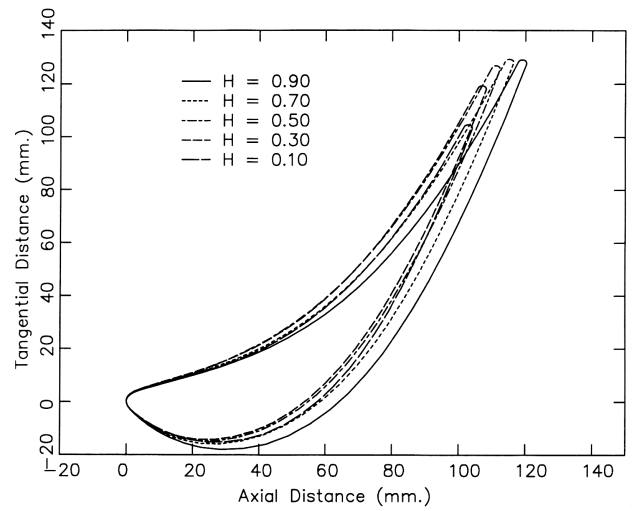


FIGURE 17: NGV five section profile.

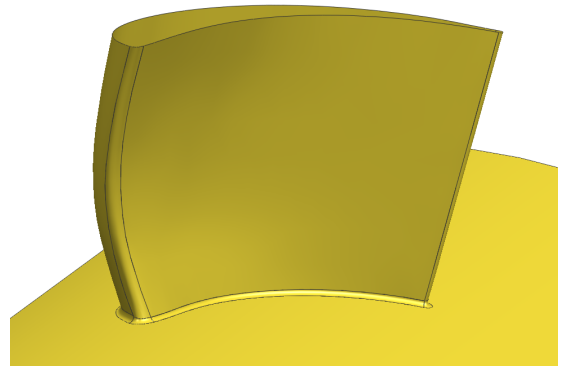


FIGURE 18: NGV solid model.

Appendix B: Experimental Data Uncertainty

In this paper, the computational results are compared with the experimental data of Zaccaria [14] obtained in Axial Flow Turbine Research Facility, AFTRF, of our laboratory.

The turbulence intensity is measured using a single sensor hot wire at one chord upstream of the NGV leading edge. The calculated total uncertainty for hot wire measurements is documented as 1.9% in measured turbulence intensity.

The nozzle guide vane exit flow is measured with a five hole probe. The percentage uncertainty for velocities are listed as 0.6% for V , 2.5% for V_x , 0.5% for V_θ , and 22% for V_r . The uncertainties for total pressure and static pressure are calculated as 30 Pa and 33 Pa, respectively.